Xiaojie Liu · Chaoying Zhao · Qin Zhang · Chengsheng Yang · Wu Zhu

Heifangtai loess landslide type and failure mode analysis with ascending and descending Spot-mode TerraSAR-X datasets

Abstract The Heifangtai loess terrace in northwest China is a well-known area to study loess landslides because of its frequent occurrence, various types, and complex trigger factors. The determination of loess landslide type and failure mode is of great significance for the landslide risk assessment, hazard mitigation, and prevention. In this study, ascending and descending Spot-mode TerraSAR-X datasets are employed to analyze the deformation patterns and failure modes of loess landslides in Xinyuan landslide group, Heifangtai terrace, by using multidimensional small baseline subsets (MSBAS) technique. First, the locations of three active landslides are delineated by independent InSAR observations from both ascending and descending TerraSAR-X datasets. Then, two-dimensional deformation rates and time series results in both vertical and horizontal east-west directions of the identified landslides are calculated using MSBAS technique. Finally, the deformation types and failure modes of landslides in the study sites are analyzed by jointly using the two-dimensional deformation rates and time series results, topographic map, remote sensing images, and previous studies on the loess landslide failure modes. With the aid of complementary data including topographic map, remote sensing image, previous studies on the loess landslide failure modes, and field investigations, two-dimensional deformation results derived from ascending and descending SAR images are compatible with three typical failure modes of loess landslide including loess-bedrock planar slide, retrogressive failure, and loess slide. Furthermore, the two-dimensional deformation derived from InSAR technique can give much detailed deformation characteristics and movement of loess landslide.

Keywords Loess landslide · Heifangtai · Failure modes · InSAR · Multidimensional small baseline subsets (MSBAS)

Introduction

Landslides are widely distributed in the world and cause enormous direct and indirect damages each year. The loess plateau, located in northwest China, is the most concentrated and largest loess area in the world. In the past decades, landslide disasters occurred on the loess plateau have caused enormous casualties and huge economic losses. Heifangtai loess terrace (13.7 km²), as a well-known loess landslides area, has about 200 landslides distributed on the edge of the terrace caused by heavy agricultural irrigations (Peng et al. 2017).

It is of great significance to find efficient and reliable methods to analyze the deformation pattern and failure mode of loess landslide for effective disaster assessment and prevention. Nowadays, four methods are mainly focused on the study of deformation pattern and failure mode of loess landslide, i.e., field geological investigations, in-situ monitoring and tests, aerial photographs, and laboratory experiments. Peng et al. (2015) studied the moving characteristics of loess landslide in Tianshui city triggered by continuous and heavy precipitation based on aerial photograph interpretation, field mapping, three-dimensional laser scanning, and laboratory tests. Qi et al. (2017) analyzed the failure mechanism of loess flow slides and the characteristic of slope retreat in Heifangtai terrace based on field investigations and monitoring, aerial and remote sensing images, and laboratory experiments. These methods are becoming very challenging when they are applied in the large-area loess landslide analysis due to the high cost and low efficiency.

On the contrary, the spaceborne Synthetic Aperture Radar (SAR) interferometry (InSAR) technique is characterized by large spatial coverage and high sensitivity to the deformation of the earth's surface, which has been widely used in the landslide investigation (Zhao et al. 2012; Iglesias et al. 2015a, 2015b; Kang et al. 2017; Zhao et al. 2018a; Bru et al. 2018; Zhao et al. 2018b). As most landslides move along both horizontal and vertical directions (He et al. 2015), the classical InSAR technique including Stacking-InSAR (Lyons and Sandwell 2003), PS-InSAR (Ferretti et al. 2001), and SBAS-InSAR (Berardino et al. 2002) can only obtain one-dimensional deformation along the line-of-sight (LOS) direction. There still exist several limitations in the detailed landslide investigation, such as (1) it is challenging to analyze the deformation mechanism of landslide and easy to misunderstand it in case of a complex situation; (2) it is hard to observe the deformation which is orthogonal to the LOS direction. Therefore, two- and/or three-dimensional surface deformation monitoring technique is on high demand.

With the increasing availability of multi-tracking SAR data, some advanced two and/or three-dimensional InSAR deformation monitoring techniques have been developed, which allow us to have an intensive understanding for the landslide deformation characteristics and make it possible to study the landslide deformation type and failure mode. Liu et al. (2013) calculated two-dimensional deformation rates for both north and vertical directions of Huangtupo landslide in China using ascending and descending Envisat SAR images. Singleton et al. (2014) employed sub-pixel offset time series technique to monitor two-dimensional movements of Shuping landslide in the Three Gorges region, China. He et al. (2015) performed a feasibility study of the large-scale landslide two-dimensional monitoring in Fushun west open-pit mine of China by combining multi-aperture InSAR (MAI) and DInSAR.

Loess landslides are characterized by small spatial extent and small deformation magnitude (Zhao et al. 2016). The abovementioned offset-tracking and MAI methods are overall not applicable for two- and/or three-dimensional deformation

monitoring of loess landslides due to the low measurement accuracy (between 1/10 and 1/30 pixels size) (Hu et al. 2014) and large gradient deformation requirement (Jung et al. 2009). In this study, Spot-mode ascending and descending TerraSAR-X images are involved and a multidimensional small baseline subset (MSBAS) technique (Samsonov et al. 2013) is employed to recover the two-dimensional deformation rates and time series deformation of loess landslides in both east-west and vertical directions. Three typical failure modes of loess landslide are then analyzed based on the obtained two-dimensional deformation results, topographic map, remote sensing images, and previous studies. The reliability of the obtained results is verified and evaluated by field geological survey.

Study area and SAR datasets

Study area

Heifangtai loess terrace (Fig. 1) is taken as the study area, which is located at 42 km west of Lanzhou, Gansu province, China. It comprises two terraces, that is Heitai and Fangtai. Due to the strong uplift of the adjacent Tibetan Plateau, the early gullies and the Yellow River cut down into the pre-Pleistocene (Cretaceous) bedrocks, which results in the formation of rock-seated river terraces (i.e., Heifangtai terrace) (Liu 1985). During this process, fluvial deposits remained on the surface of the bedrocks. At the time of upper Pleistocene, the loess transported by wind fell and settled down on the terrace (Xu et al. 2014). Therefore, the engineering geology of Heifangtai terrace can be divided into four units as shown in Fig. 2 (Qi et al. 2017), including from the top to the bottom of Manlan loess (Q_3^{eol}) with a thickness of approximately 26–48 m, a low permeability alluvial clay layer (Q_3^{al}) with about 3 to 19 m thick, an underlying layer of fluvial gravel (Q_3^{al}) mixed with sands about 1 to 6 m thick, and bedrocks (K_1hk) consist of sandstone partings with a dip angle of about 8–12° and dip direction of about 125–220°.

The average annual evaporation capacity is about 5.4 times the precipitation in the terrace (Zeng et al. 2016). Therefore, a large amount of water has been pumped from the Yellow River for agricultural irrigation on the surface of the terrace (Fig. 1b). As a result, the groundwater level of Heifangtai terrace has significantly increased, which caused dense cracks and loess landslides (about 200 landslides) along the edge of the terrace (Peng et al. 2017). Liu et al. (2018) identified about 48 active loess landslides distributed along the edge of Heifangtai terrace from 2016 to 2017 using multisource SAR datasets, which are divided into nine landslide groups. Xinyuan landslide group is chosen as the test site to investigate the deformation characteristic and failure mode of loess landslide owing to its visibility for both ascending and descending SAR data. Peng et al. (2017) summarized five failure modes of loess landslide in Heifangtai terrace based on aerial images, digital elevation model (DEM), and field investigations, that is loess-bedrock planar slide, loess-bedrock irregular slide, loess flow slide, loess slide, and loess flow. The deformation data involved in the study were obtained from the single-point crack measurements and the difference of unmanned aerial vehicle (UAV) DEMs. Given the small deformation magnitude of the loess landslides and the low height accuracy of the UAV DEMs, it is challengeable to monitor them with the method of UAV DEM difference.

SAR datasets

In order to accurately monitor the deformation of small-scale loess landslides in Heifangtai terrace, high-resolution SAR datasets from both ascending and descending Spot-mode TerraSAR-X are collected. In total, 23 ascending SAR images acquired with track 21 from February 2016 to November 2016, and 19 descending SAR images acquired with track 165 from January 2016 to November 2016 are used. The basic parameters for two SAR datasets are listed in Table 1, while their coverages are shown in Fig. 1a. According to the special characteristics of loess landslides, i.e., small spatial extent, and to meet the requirement of high-resolution SAR data processing, the UAV DEM with 3-m spatial resolution is used to remove the topographic phase from the SAR interferograms.

All interferograms with the temporal baseline less than 60 days and the perpendicular baseline less than 250 m are generated. The multilooking factors of 2× 2 for the interferograms are set to decrease the influences of the decorrelation; hence, the spatial spacing of the multi-looked interferograms is about 3 m in both range and azimuth directions. Then, interferograms contaminated by heavy decorrelation due to dense vegetation and heavy rainfall in the summer season are excluded for the following processing. Finally, a total of 60 high-quality interferograms including 33 ascending and 27 descending tracks are left, which are shown in Fig. 3.

Methodology

Calculation of two-dimensional deformation rates and time series

As single SAR datasets can only get the surface deformation in the LOS direction, it can hardly retrieve more than one-dimensional surface deformation simultaneously. An advanced multidimensional small baseline subset (MSBAS) technique was developed to combine multiple DInSAR datasets to generate multidimensional surface deformation with dense temporal sampling and low noise (Samsonov and d'Oreye 2012). Once ascending and descending SAR datasets have time overlap for their acquisition periods, MSBAS can produce denser time series deformation than each individual SAR datasets. The problem of data redundancy and multidimensionality is addressed in MSBAS processing by decomposing one-dimensional LOS deformation into the vertical and horizontal east-west directions using ascending and descending SAR images.

When a single SAR dataset acquired by one sensor with an incidence angle θ and azimuth α, the time series deformation can be retrieved by the SBAS method (Berardino et al. 2002):

$$BV_{\mathrm{los}} = \phi_{\mathrm{obs}}; V_{\mathrm{los}} = B^+\phi_{\mathrm{obs}}; d_{\mathrm{los}}^i = d_{\mathrm{los}}^{i-1} + V_{\mathrm{los}}^i \Delta t^i \qquad (1)$$

where B is an $M \times N$ matrix (M is the number of interferograms and $N + 1$ is the number of SAR images), V_{los} represents the LOS average deformation rates, ϕ_{obs} represents the observed interferometric phases, B^+ is a pseudo-inverse of matrix B calculated by applying the singular value decomposition (SVD), and d_{los}^i is the LOS displacement at the epoch t^i.

In case of K multiple SAR datasets acquired by different sensors with different incidence angles and azimuths, the Eq. (1) can be
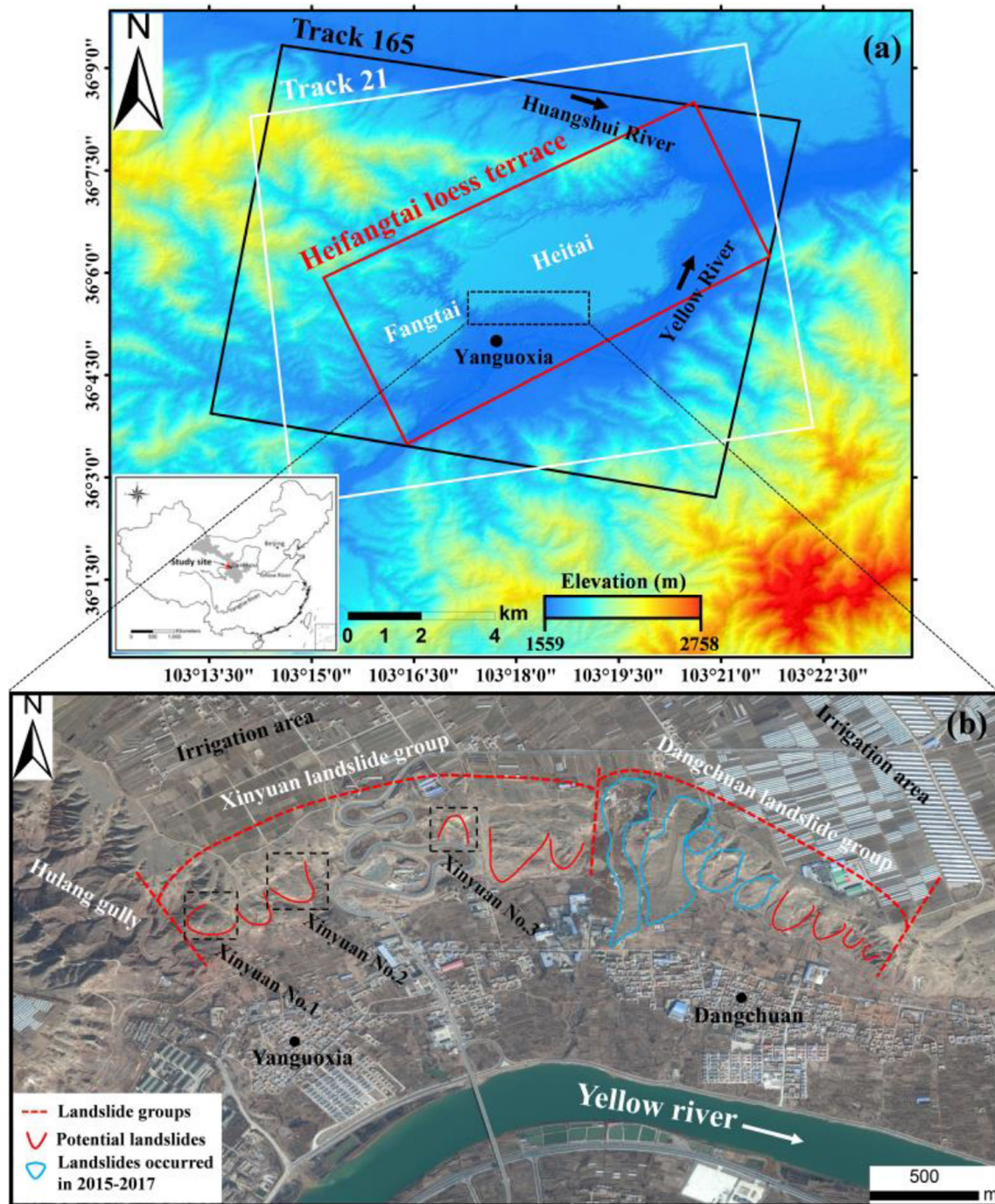
Fig. 1 Study area and SAR datasets coverage. **a** Location of the study area indicated by the red rectangle. The black and white rectangles show the coverage of the descending (track 165) and ascending (track 21) Spot-mode TerraSAR-X data. **b** Landsat-8 remote sensing image of the zoomed study area acquired in February 2017

rewritten in the following form for each dataset $k = 1 \cdots K$ (Samsonov et al. [2013]):

assuming,

$$\left| S_N^k B \ S_E^k B \ S_U^k B \right| \cdot \left| V_N \ V_E \ V_U \right|^{\mathrm{T}} = \phi_{\mathrm{obs}}^k \qquad (2)$$

$$V_{los} = SV = S_N V_N + S_E V_E + S_U V_U \qquad (3)$$
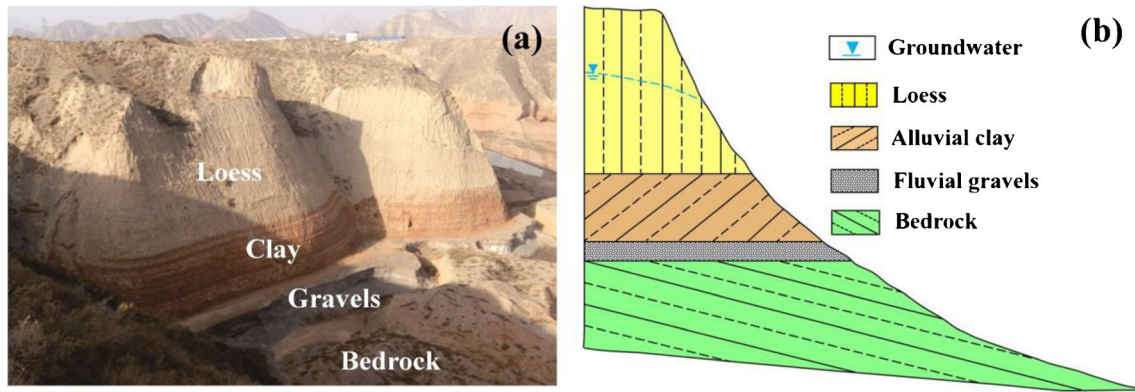
Fig. 2 Geological profile of Heifangtai loess terrace (revised after Qi et al. 2017 and Peng et al. 2017). **a** Scenic photo of a representative slope. **b** Geological profile

$$S = \{S_N, S_E, S_U\} = \{\sin\alpha\sin\theta, -\cos\alpha\sin\theta, \cos\theta\} \quad (4)$$

where S is a unit vector of LOS with north, east and up components S_N, S_E, S_U, and V is a deformation rate vector with components V_N, V_E, and V_U.

Therefore, the MSBAS approach can be expressed in the following equation once all K independent SAR datasets are involved:

$$\begin{pmatrix} B^1 \\ B^2 \\ --- \\ B^K \end{pmatrix} \times \begin{pmatrix} V_N \\ V_E \\ V_U \end{pmatrix} = \begin{pmatrix} \phi^1 \\ \phi^2 \\ --- \\ \phi^K \end{pmatrix} \text{ or } \hat{B}\hat{V}_{los} = \hat{\phi}_{obs} \quad (5)$$

where $\hat{B}$ is a new matrix with $3\left(\sum\limits_{k=1}^{K} N^k - 1\right) \times \sum\limits_{k=1}^{K} M^k$ dimensions, $\hat{V}$ is a new unknown velocity vector with dimensions $1 \times 3\left(\sum\limits_{k=1}^{K} N^k - 1\right)$, and $\hat{\phi}_{obs}$ is a new observation vector with $1 \times \sum\limits_{k=1}^{K} M^k$ dimensions. The near-polar orbit spaceborne SAR satellite can acquire data insensitive to the motion in the north-south direction due to its inherent SAR geometry (Samsonov et al. 2013). For TerraSAR data listed in Table 1, the contributions of the real three-dimensional (i.e., north-south, east-west, and vertical) ground deformation projection to the LOS direction are about 11%, 65%, and 75%, respectively. Therefore, the contribution of the north-south direction can be neglected in general (Samsonov

and d'Oreye 2017). Equation (5) can be further simplified by excluding the north-south component V_N and thereby, the dimensions of matrix $\hat{B}$ can be reduced to $2\left(\sum\limits_{k=1}^{K} N^k - 1\right) \times \sum\limits_{k=1}^{K} M^k$. Equation (5) is rank deficient because the number of unknown parameters is greater than the number of linearly independent equations. It can be solved by using the SVD and the zero-, first-, or second-order Tikhonov regularization (Samsonov and d'Oreye 2017). Two-dimensional time series deformation can be retrieved from the obtained deformation rates by numerical integration using the following equation:

$$d_p^U = \sum\limits_{i=1}^{p} V_i^U \Delta t; d_p^E = \sum\limits_{i=1}^{p} V_i^E \Delta t_i \quad (6)$$

where $p = 1, 2, 3, ..., \sum_{k=1}^{K} N^k$, d_p^U, and d_p^E are the cumulative vertical and horizontal east-west deformations, respectively.

Analysis of loess landslide types and failure modes

The detailed flowchart of loess landslide type and failure mode analysis is depicted in Fig. 4 based on InSAR technique and complementary data. First, ascending and descending SAR datasets covering common period and region are acquired with different SAR acquisition parameters, including incidence angle and azimuth. Then, for each SAR dataset, the SAR images are first co-registered. All possible interferograms are generated, filtered (Goldstein and Werner 1998), and unwrapped (Costantini 1998). The artifacts of atmospheric disturbance, residual baseline effects,

Table 1 Basic parameters of the SAR datasets used in this study

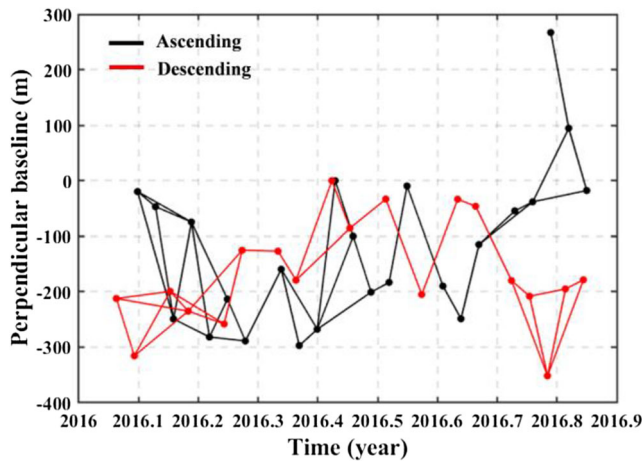| SAR sensor	TerraSAR-X	TerraSAR-X
Track	21	165
Orbit direction	Ascending	Descending
Incidence angle (°)	41.2	41.8
Azimuth angle (°)	− 9.7	189.6
Resolution (azimuth × range)	1.26 m × 0.91 m	1.26 m × 0.91 m
Number of SAR images	23	19
Acquisition period	20160206–20161107	20160124–20161105

Fig. 3 Temporal and perpendicular baseline of selected ascending (black line) and descending (red line) TerraSAR-X interferograms in this study

and the residual topographic errors are reduced using a combined biquadratic and linear model (Kang et al. 2017). Eventually, high-quality unwrapped interferograms from different SAR tracks are geocoded and resampled to a common grid of longitude and latitude to calculate two-dimensional deformation rates and time series using the Tikhonov regularization (Samsonov et al. 2017). Finally, the loess landslide types and failure modes are analyzed based on the deformation characteristics, topographic map, remote sensing images, and previous studies on the loess landslide failure modes.

It is worth noting that the selection of regularization order depends on the objectives of the study and the characteristics of the signal. If the average deformation rate of the study objectives is close to zero (e.g., oscillating motion), the zero-order regularization should be adopted, while the first- and second-order regularizations are suitable for measuring a steady moving objective (Samsonov and d'Oreye 2017).
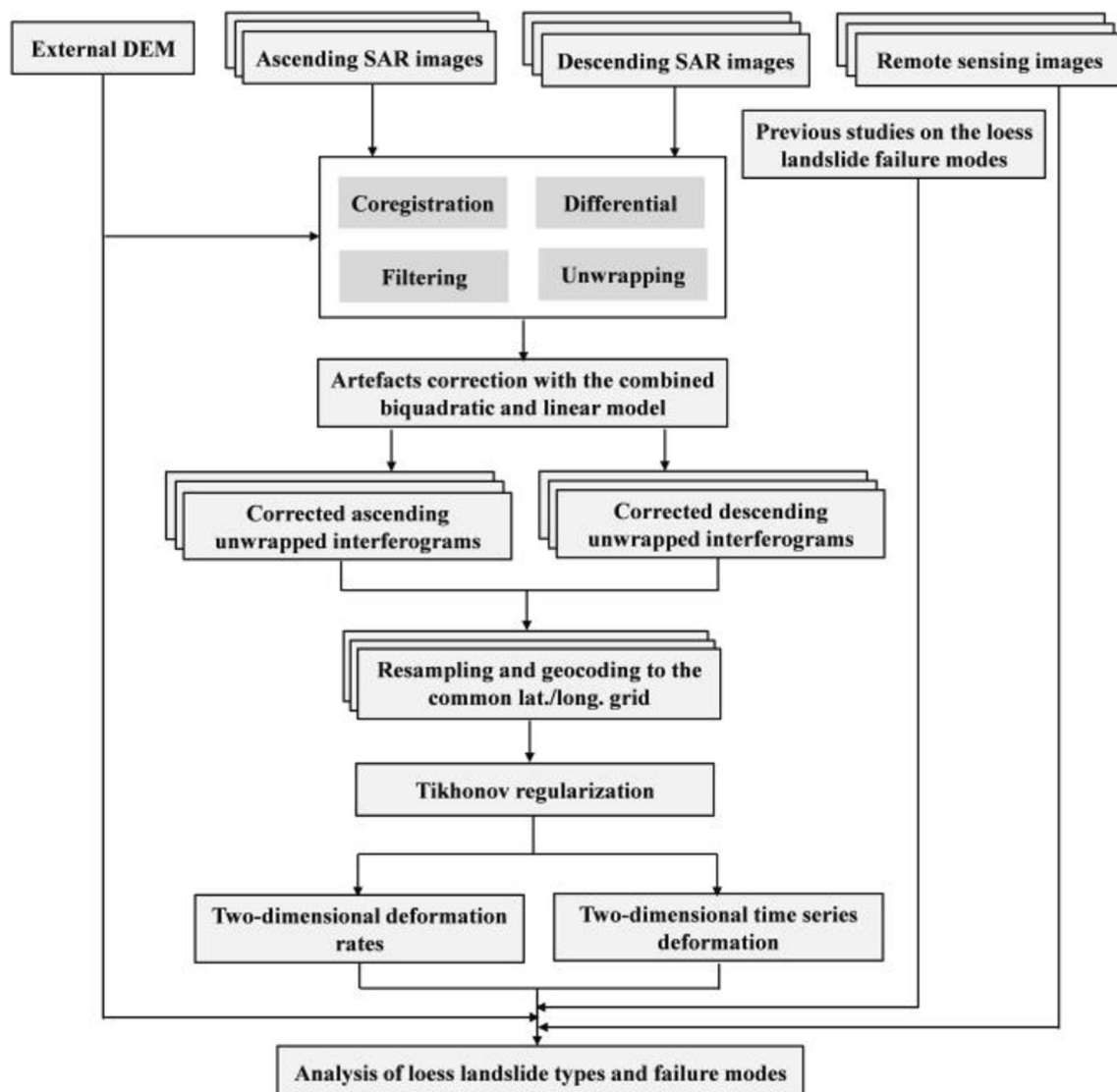

Fig. 4 Flowchart of loess landslide type and failure mode analysis with InSAR technique
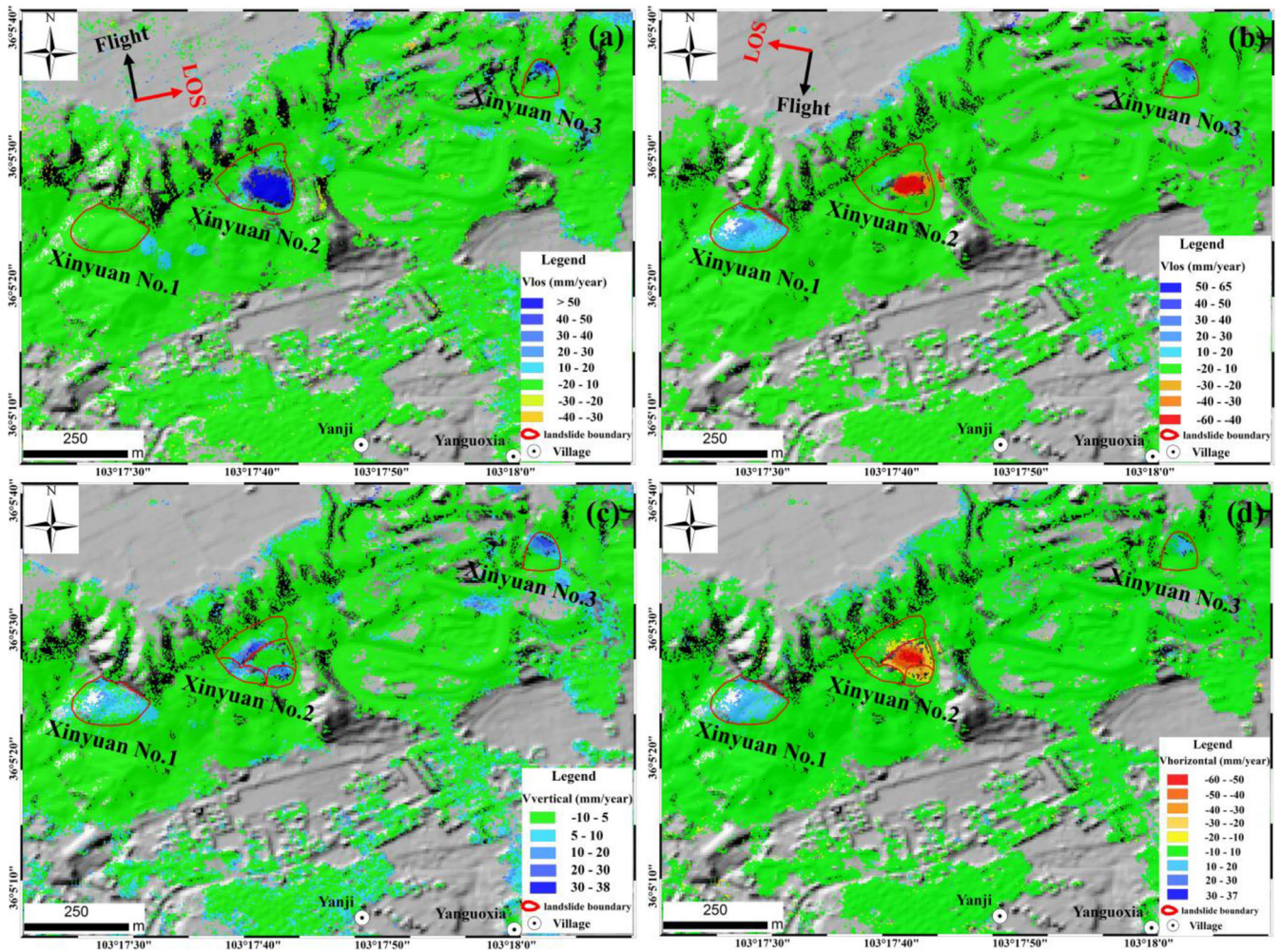
Fig. 5 Average deformation rate maps over the whole Xinyuan landslide group of Heifangtai terrace. **a** Average deformation rate map from track 21 (ascending) from February 2016 to November 2016. **b** Average deformation rate map from track 165 (descending) from January 2016 to November 2016. **c** Vertical deformation rate map. **d** Horizontal east-west deformation rate map

Results and discussions

One-dimensional LOS average deformation rates for each pixel for the ascending and descending datasets were calculated individually by weighted averaging of the high-quality interferograms (i.e., stacking; Lyons and Sandwell 2003), as shown in Fig. 5a, b. Note that positive value indicates the displacement away
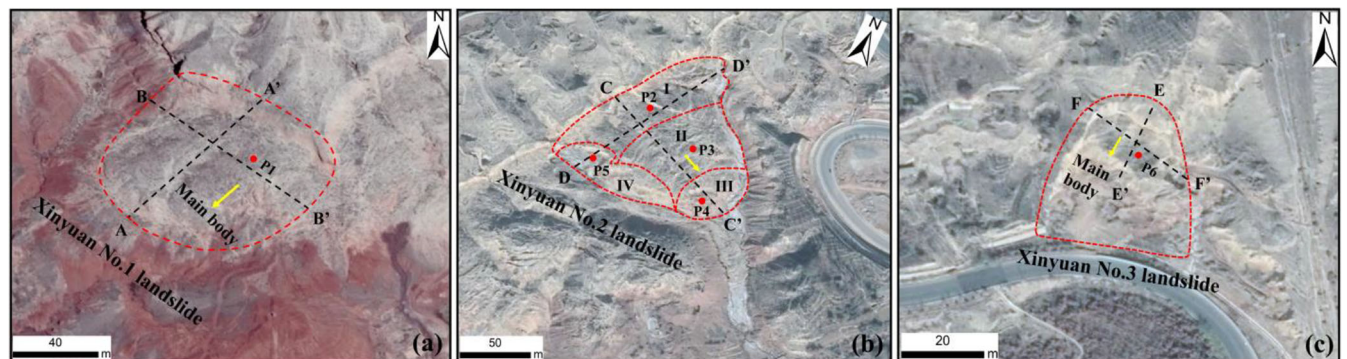

Fig. 6 Landsat-8 remote sensing images of Xinyuan no. 1 (**a**), no. 2 (**b**), and no. 3 (**c**) landslides acquired on 12 November 2017. The red dotted lines indicate the boundary of the landslides, and the yellow arrows indicate the main sliding direction. Dashed lines indicate the location of deformation profiles, and red dots show the location of InSAR time series deformation
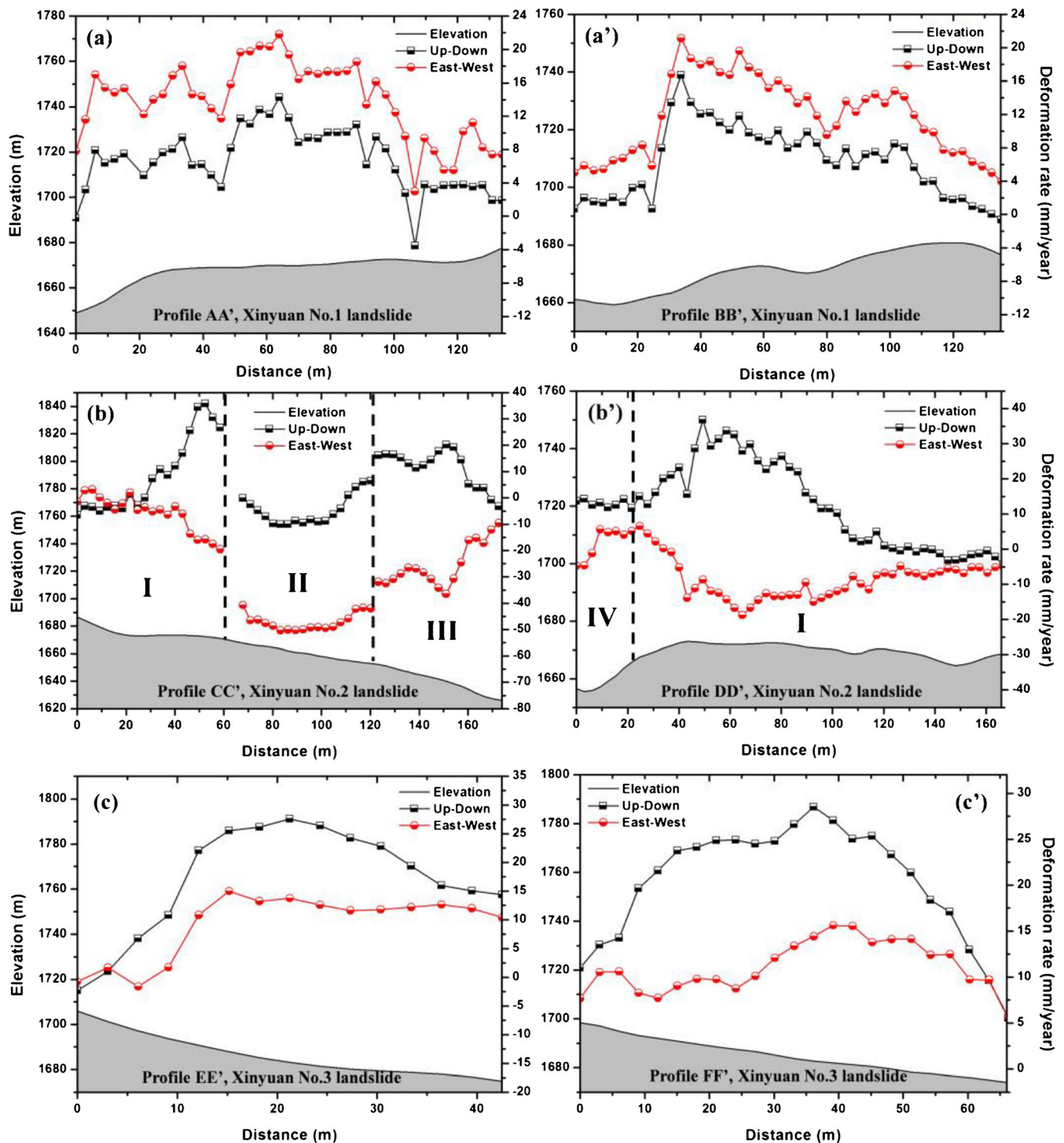
Fig. 7 Two-dimensional deformation rates from January 2016 to November 2016 and elevation of Xinyuan no. 1, no. 2, and no. 3 landslides along the profiles of AA' – FF'; the locations of the profiles of AA' – FF' are marked in Fig. 6

from the sensor and negative value represents the displacement towards the sensor. Two-dimensional deformation rates and time series are retrieved based on Eqs. (5) and (6). The first-order regularization is used in this study. The vertical and horizontal east-west deformation rate maps over the whole Xinyuan landslide group of Heifangtai terrace are shown in Fig. 5 c and d, respectively. It can be seen from Fig. 5a, b that the deformation extent and magnitude of landslides measured by ascending and descending data show a big difference due to the different imaging geometries. Two potential loess landslides namely Xinyuan no. 2 and no. 3 are successfully identified by both deformation maps from ascending and descending SAR data, while Xinyuan no. 1
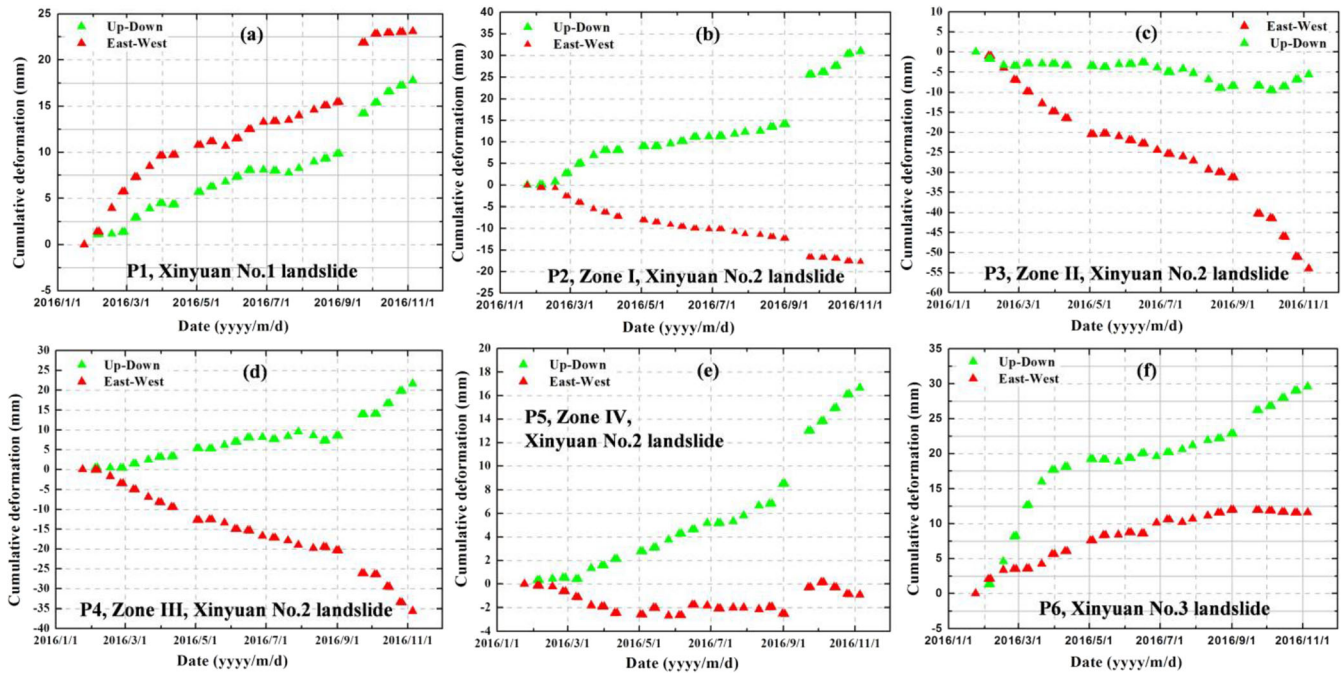
Fig. 8 Two-dimensional time series deformation of Xinyuan no. 1, no. 2, and no. 3 landslides for points P1-P6 marked in Fig. 6

landslide is only detected by descending SAR data. As for the ascending geometry of Xinyuan no. 1 landslide, the LOS deformation projected from the vertical component and east-west component is around zero. It is proved that ascending and descending SAR data are complementary for the potential landslide identification. Moreover, the different deformation feature for Xingyuan no. 2 landslide can be explained as the different sensitivities of the ascending and descending SAR data to the specific landslide deformation. The maximum deformation rate in LOS direction is measured by descending data in the Xinyuan no. 2 as − 60 mm/ year. The maximum deformation rates in vertical and east-west directions for three landslides are 22 mm/year and 28 mm/year, 38 mm/year and − 60 mm/year, and 30 mm/year and 20 mm/year, respectively.

Xinyuan no. 1 landslide is located on the left side of Hulang gully, Xinyuan no. 2 landslide is located in Xinyuan village, and Xinyuan no. 3 landslide is located on the north side of Zheda road, Heifangtai. The full views of the three landslides are shown on Landsat-8 remote sensing images acquired on 12 November 2017 in Fig. 6. The lengths of three landslides are about 130 m, 170 m, and 86 m, respectively, and the widths are about 135 m, 165 m, and 50 m, respectively. Two-dimensional deformation rates and elevation of the three landslides are extracted along six profiles of AA'-FF' to analyze the deformation characteristics of landslides in detail, as shown in Fig. 7, while two-dimensional time series deformations for points P1-P6 marked in Fig. 6 are shown in Fig. 8 to analyze the landslide evolution.

It can be clearly seen from Figs. 5c, d and 7a, a' that Xinyuan no. 1 landslide is dominated by horizontal east-west deformation (i.e., westward movement) and relatively small vertical deformation. In addition, the landslide experiences uneven deformation, which is controlled obviously by the development of cracks. It can be seen from Fig. 8a that there is a continuous horizontal deformation of

the landslide before October 2016; however, the horizontal deformation is almost unchangeable after October 2016. The landslide continues to deform in the vertical direction during the InSAR monitoring. Based on the two-dimensional deformation results, topographic map, remote sensing image, and previous studies on the loess landslide failure mode (Peng et al. 2017; Xu et al. 2014), it can be deduced that Xinyuan no. 1 landslide belongs to the loess-bedrock planar slide failure mode. For the detailed failure process and formation mechanism of the loess-bedrock planar slide, please refer to Xu et al. (2014) and Peng et al. (2017).

It can be seen from Fig. 5c, d that the whole Xinyuan no. 2 landslide moves eastward, and the vertical deformation is only observed at the edge of the landslide. The landslide can be further divided into four zones based on the two-dimensional deformation results, that is zones I, II, III, and IV, as shown in Fig. 6b. On the basis of Fig. 7 b and b', we can see (1) the deformation in vertical and east-west direction are observed simultaneously in zone I; however, the vertical deformation is larger than the one in the east-west direction; (2) there is only the east-west deformation in zone II; (3) the vertical and east-west deformations are also observed simultaneously in zone III; however, the east-west deformation is greater than the one in the vertical direction; (4) there is only the vertical deformation in zone IV; (5) the deformation along the transverse line of DD' is also controlled by the development of the cracks; as a result, abrupt deformation changes are observed across the cracks. It can be seen from Fig. 8b–e that each zone of Xinyuan no. 2 deforms continuously in the vertical and/or horizontal east-west directions from 2016 to 2017. The maximum cumulative displacement in vertical direction occurred in zone I amounting to 33 mm, and the maximum cumulative displacement in east-west direction appeared in zone II amounting to − 54 mm. Based on the two-
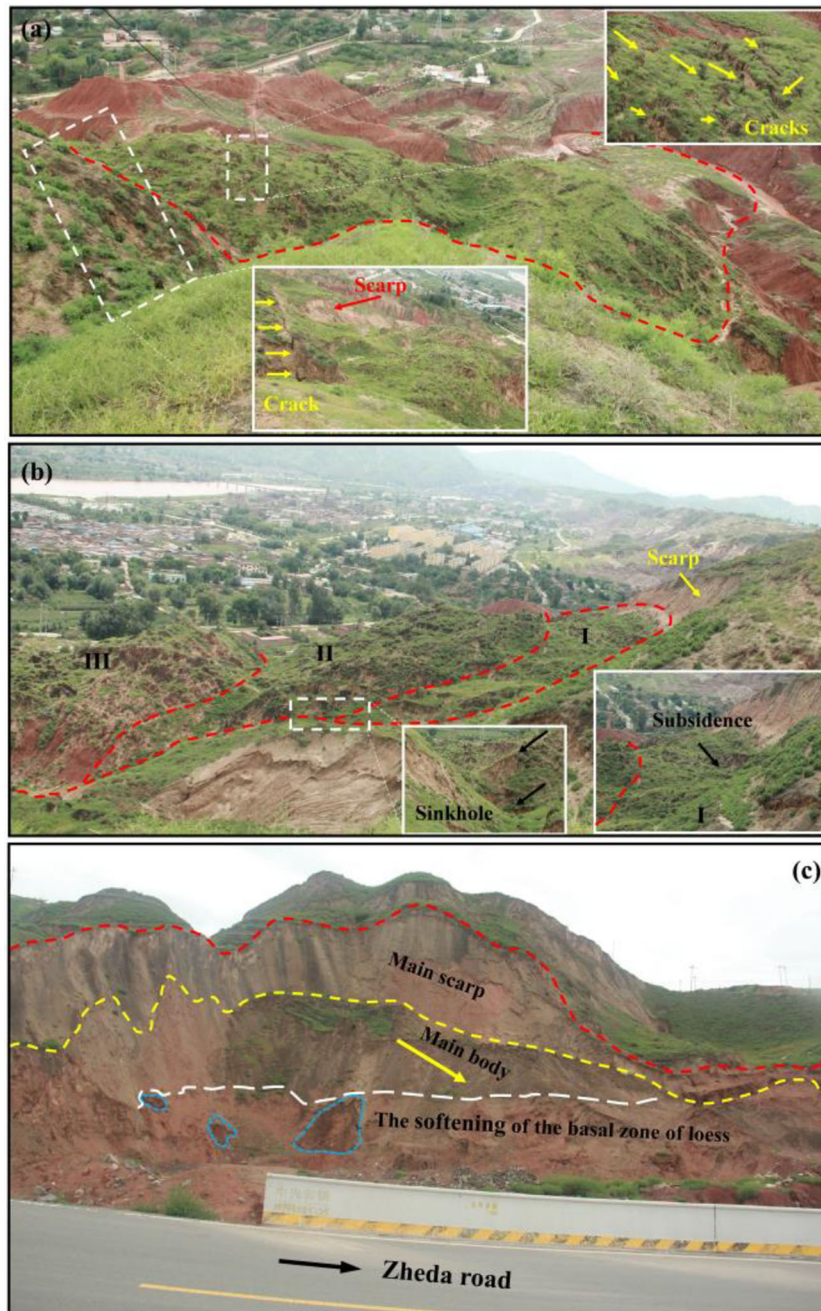
Fig. 9 Scene photos of Xinyuan no. 1 (**a**), no. 2 (**b**), and no. 3 (**c**) landslides taken in August 2018. The red dotted lines indicate the boundary of the landslides and the boundary of the zones

dimensional deformation results, topographic map, remote sensing image, and previous studies on the loess landslide failure mode (Qi et al. 2017; Cui et al. 2018), it can be deduced that Xinyuan no. 2 landslide is correlated to the retrogressive failure mode of loess landslide. A large scarp can be seen from Figs. 6b and 9b formed at the back edge of the landslide, which makes the whole landslide completely separated from the terrace. Subsequently, the retrogressive failure is started at the edge of the landslide. For the detailed failure process and formation mechanism of retrogressive

failure, please refer to Xu et al. (2012), Qi et al. (2017) and Cui et al. (2018).

Compared with Xinyuan no. 1 and no. 2 landslides, it can be seen from Fig. 5c, d that Xinyuan no. 3 landslide shows the different deformation patterns, which is dominated by the vertical deformation, along with a slight east-west deformation. In addition, Xinyuan no. 3 landslide has a smaller spatial scale than the first two landslides. It can be seen from Fig. 7c, c' that the vertical deformation in the trailing section of Xinyuan no. 3 is larger than that in the leading section.

However, the east-west deformation in the trailing section of Xinyuan no. 3 is similar to the leading section. In addition, it is evident that the deformation in the middle part of Xinyuan no. 3 is greater than that in the edge section. It can be seen from Fig.8f that Xinyuan no. 3 landslide had a large vertical deformation before April 2016, which indicates that it was undergoing major internal failure. However, the landslide turned to the stage of slow-rate deformation after April 2016, which may be closely correlated with the seasonal freeze-thaw activity of loess landslide (Cheng et al. 2013). On the basis of the obtained two-dimensional deformation results, topographic map, remote sensing image, and previous studies on the loess landslide failure mode (Peng et al. 2017; Xu et al. 2014), it can be deduced that Xinyuan no. 3 landslide belongs to the loess slide failure mode. For the detailed failure process and formation mechanism of loess slide, please refer to Xu et al. (2014) and Peng et al. (2017).

In order to verify and evaluate the deformation patterns and failure modes deduced by jointly using InSAR deformation results, topographic map, remote sensing images, and previous studies on the loess landslide failure mode, a field geological survey was conducted in August 2018. The scene photos of Xinyuan no. 1, no. 2, and no. 3 landslides are shown in Fig. 9 a, b, and c, respectively. It can be seen from Fig. 9 that two-dimensional deformation characteristics obtained by InSAR technique are in good agreement with the actual terrain of the three landslides; dense cracks and fractured surfaces were observed over the three landslide bodies. For the Xinyuan no. 1 landslide (see Fig. 9a), a crack with the width of about 10 cm was found at the back edge of the landslide (as shown in the yellow arrows in Fig. 9a), which makes the whole landslide body separated from the terrace. For Xinyuan no. 2 landslide (see Fig. 9b), the whole landslide body was cut by dense cracks to form a discontinuous broken surface. A main sliding scarp with a width of about several meters can be seen at the back edge of the landslide, and some sinkholes were found along the crack on the left side of the landslide. In addition, it is evident that the land subsidence occurred in the zone I and the trailing of zone III. For Xinyuan no. 3 landslide (see Fig. 9c), a main sliding scarp with a depth of about several meters can be observed at the back edge of the landslide. The softening of the basal zone of loess (as shown in the white dotted line in Fig. 9c) and the seepage of groundwater (as shown in the blue dotted lines in Fig. 9c) can be clearly seen above the alluvial clay layer.

Conclusions

The method of analysis of loess landslide type and failure mode is presented based on two-dimensional InSAR technique and complementary data. Xingyuan landslide group at Heifangtai loess terrace is taken as the study area to illustrate three different cases. Two-dimensional deformation rates and time series for both vertical and horizontal east-west directions are calculated using an advanced multidimensional small baseline subset (MSBAS) algorithm. Three typical loess landslide failure modes have been verified based on the two-dimensional deformation results, topographic map, remote sensing images, and previous studies on the loess landslide failure modes. Xinyuan no. 1 landslide belongs to the loess-bedrock planar slide failure mode with the characteristics of larger horizontal deformation than the vertical deformation. Xinyuan no. 2 landslide is correlated with the

retrogressive failure mode with the different horizontal and vertical deformation in different landslide zones. Xinyuan no. 3 landslide belongs to the loess slide failure mode as the deformation was dominated by vertical deformation. The reliability of the results is evaluated and verified by the field investigation and documented files.

In addition, MSBAS method outperforms one-dimensional DInSAR technique in the following two aspects: (1) higher temporal resolution time series results can help us to capture the accelerated deformation and make an almost early warning for the specific landslide; (2) different landslide failure modes can help us to assess the landslide risk and provide the appropriate mitigation measures.

In this study, the north-south component of landslide deformation is less sensitive than the other two components and it is neglected in the processing of MSBAS. However, it will become very important and cannot be neglected when some landslides suffer large north-south deformation. In that case, three-dimensional surface deformation of landslide should be considered.

References

Berardino P, Fornaro G, Lanari R, Sansosti E (2002) A new algorithm for surface deformation monitoring based on small baseline differential SAR interferograms. IEEE Trans Geosci Remote Sens 40:2375–2383

Bru G, Escayo J, Fernández J, Mallorqui J, Iglesias R, Sansosti E, Abajo T, Morales A (2018) Suitability assessment of X-band satellite SAR data for geotechnical monitoring of site scale slow moving landslides. Remote Sens 10:936

Cheng X, Zhang M, Zhu L, Pei Y, Li Z, Hu W (2013) Seasonal freeze-thaw action and its effect on the slope soil strength in Heifangtai area, Gansu Province. Geol Bull China 32:904–909 (In Chinese)

Costantini M (1998) A novel phase unwrapping mothed based on network programming. IEEE Trans Geosci Remote Sens 36:813–821

Cui S, Pei X, Wu H, Huang R (2018) Centrifuge model test of an irrigation-induced loess landslide in the Heifangtai loess platform, Northwest China. J Mt Sci 15:130–143

Ferretti A, Prati C, Rocca F (2001) Permanent scatterers in SAR interferometry. IEEE Trans. Geosci. Remote Sens 39:8–20

Goldstein R, Werner C (1998) Radar interferogram filtering for geophysical applications. Geophys Res Lett 25:4035–4038

He L, Wu L, Liu S, Wang Z, Su C, Liu S (2015) Mapping two-dimensional deformation field time-series of large slope by coupling DInSAR-SBAS with MAI-SBAS. Remote Sens 7:12440–12458

Hu J, Li Z, Ding X, Zhu J, Zhang L, Sun Q (2014) Resolving three-dimensional surface displacements from InSAR measurements: a review. Earth Sci Rev 133:1–17

Iglesias R, Mallorqui J, Modells D, López-Martínez C, Fabregas X, Aguasca A, Gili J, Corominas J (2015a) PSI deformation map retrieval by means of temporal sublook coherence on reduced sets of SAR images. Remote Sens 7:530–563

Iglesias R, Monells D, López-Martínez C, Mallorqui J, Fabregas X, Aguasca A (2015b) Polarimetric optimization of temporal sublook coherence for DInSAR applications. IEEE Geosci Remote Sens Lett 12:87–91

Jung H, Won J, Kim S (2009) An improvement of the performance of multiple-aperture SAR interferometry (MAI). IEEE Trans. Geosci. Remote Sens 47:2859–2869

Kang Y, Zhao C, Zhang Q, Lu Z, Li B (2017) Application of InSAR techniques to an analysis of the Guanling landslide. Remote Sens 9:1–17

Liu T (1985) Loess and the environment. China Ocean Press 1985:1–481 (In Chinese)

Liu P, Li Z, Hoey T, Kincal C, Zhang J, Zeng Q, Muller J (2013) Using advanced InSAR time series techniques to monitoring landslide movements in Badong of the Three Gorges region, China. Int J Appl Earth Obs Geoinf 21:253–264

Liu X, Zhao C, Qin Z, Peng J, Zhu W, Lu Z (2018) Multi-temporal loess landslide inventory mapping with C-, X- and L-band SAR datasets—a case study of Heifangtai loess landslides, China. Remote Sens 10:1756

Lyons S, Sandwell D (2003) Fault creep along the southern San Andreas from interferometric synthetic aperture radar, permanent scatterers, and stacking. J Geophys Res Solid Earth 108

Peng D, Xu Q, Liu F, He Y, Zhang S, Qi X, Zhao K, Zhang X (2017) Distribution and failure modes of the landslides in Heitai terrace, China. Eng Geol:1–14

Peng J, Fan Z, Wu D, Zhuang J, Dai F, Chen W, Zhao C (2015) Heavy rainfall triggered loess-mudstone landslide and subsequent debris flow in Tianshui, China. Eng Geol 186:79–90

Qi X, Xu Q, Liu F (2017) Analysis of retrogressive loess flowslides in Heifangtai, China. Eng Geol:1–10

Samsonov S, d'Oreye N (2012) Multidimensional time series analysis of ground deformation from multiple InSAR data sets applied to Virunga Volcanic Province. Geophys J Int 191:1095–1108

Samsonov S, d'Oreye N (2017) Multidimensional small baseline subset (MSBAS) for two-dimensional deformation analysis: case study Mexico City. Can J Remote Sens 43:1–12

Samsonov S, d'Oreye N, Smets B (2013) Ground deformation associated with post-mining activity at the French-German border revealed by novel InSAR time series method. Int J Appl Earth Obs Geoinf 23:142–154

Samsonov S, Feng W, Peltier A, Geirsson H, d'Oreye N, Tiampo K (2017) Multidimensional small baseline subset (MSBAS) for volcano monitoring in two dimensions: opportunities and challenges. Case study Piton de la Fournaise volcano. J Volcanol Geotherm Res 06077:1–18

Singleton A, Li Z, Hoey T, Muller J (2014) Evaluation sub-pixel offset techniques as an alternative to D-InSAR for monitoring episodic landslide movements in vegetated terrain. Remote Sens Environ 147:133–144

Xu L, Dai F, Tham L, Zhou Y, Wu C (2012) Investigating landslide-related cracks along the edge of two loess platforms in Northwest China. Earth Surf Process Landf 37:1023–1033

Xu L, Dai F, Tu X, Tham L, Zhou Y, Iqbal J (2014) Landslides in a loess platform, North-West China. Landslides 11:993–1005

Zeng R, Meng X, Zhang F, Wang S, Cui Z, Zhang M, Zhang Y, Chen G (2016) Characterizing hydrological processes on loess slopes using electrical resistivity tomography- a case study of the Heifangtai terrace, Northwest China. J Hydrol 541:742–753

Zhao C, Kang Y, Zhang Q, Lu Z, Li B (2018a) Landslide identification and monitoring along the Jinsha river catchment (Wudongde reservoir area), China, using the InSAR method. Remote Sens 10:993

Zhao C, Lu Z, Zhang Q, Fuente J (2012) Large-area landslide detection and monitoring with ALOS/PALSAR imagery data over Northern California and Southern Oregon, USA. Remote Sens Environ 124:348–359

Zhao C, Zhang Q, He Y, Peng J, Yang C, Kang Y (2016) Small-scale loess landslide monitoring with small baseline subsets interferometric synthetic aperture radar technique—case study of Xingyuan landslide, Shaanxi, China. J Appl Remote Sens 10:1–14

Zhao F, Mallorqui J, Iglesias R, Gili J, Corominas J (2018b) Landslide monitoring using multi-temporal SAR interferometry with advanced persistent scatterers identified methods and super high-spatial resolution TerraSAR-X images. Remote Sens 10:921

X. Liu · C. Zhao (✉) · Q. Zhang (✉) · C. Yang · W. Zhu
School of Geological Engineering and Geomatics,
Chang'an University,
Xi'an, 710054, People's Republic of China
Email: zhaochaoying@163.com
Email: zhangqinle@263.net.cn

C. Zhao · Q. Zhang · C. Yang · W. Zhu
National Administration of Surveying, Mapping and Geoinformation, Engineering Research Center of National Geographic Conditions Monitoring,
Xi'an, 710054, People's Republic of China